Clays and Clay Minerals, Vol. 55, No. 1, 1–17, 2007.

CHARACTERIZATION OF ALTERATION PRODUCTS IN TEPHRA FROM HALEAKALA, MAUI: A VISIBLE-INFRARED SPECTROSCOPY, MÖSSBAUER SPECTROSCOPY, XRD, EMPA AND TEM STUDY

JANICE L. BISHOP[1,2,*], PETER SCHIFFMAN[3], ENVER MURAD[4], M. DARBY DYAR[5], AHMED DRIEF[3,6] AND MELISSA D. LANE[7]

[1] SETI Institute, 515 N. Whisman Road, Mountain View, CA 94043, USA
[2] NASA-Ames Research Center, Mail Stop 239-4, Moffett Field, CA 94035, USA
[3] Department of Geology, University of California, Davis, CA 95616, USA
[4] Bayerisches Landesamt für Umwelt, Leopoldstr. 30, Postfach 389, D-95603 Marktredwitz, Germany
[5] Mount Holyoke College, 50 College Street, South Hadley, MA 01075, USA
[6] The Clorox Company, 7200 Johnson Drive, Pleasanton, CA 94588, USA
[7] Planetary Science Institute, 1700 E. Fort Lowell, Suite 106, Tucson, AZ 85719, USA

Abstract—Altered basaltic tephra from Haleakala, Maui, are characterized using multiple techniques in order to identify the minerals formed under a variety of conditions and to understand the soil formation processes here. We collected samples that are representative of typical bulk weathered material in the crater, as well as solfataric alteration in a hydrothermal environment. For this study X-ray diffraction, electron probe microanalysis, scanning electron microscopy and transmission electron microscopy are coupled with spectroscopic techniques including Mössbauer, visible-infrared reflectance, transmission infrared, and thermal infrared emission spectroscopies to analyze these samples. The unaltered tephra are composed of feldspar, glass, pyroxene and olivine. Observed alteration products include Fe oxides, phyllosilicates and sulfates, as well as SAED amorphous Al-Si-bearing material. These samples are potential analogs for altered volcanic material on Mars as the pedogenic influences and contact with plants and animals are minimal. Results from this study may help to determine spectral signatures of these samples that could be used for identification on Mars of the minerals observed here.

Key Words—Altered Tephra, Alunite, EMPA, Infrared Spectroscopy, Jarosite, Mars, Mössbauer, SEM, Smectite, Solfataric Alteration, XRD.

INTRODUCTION

Haleakala is a basaltic volcano located on the island of Maui near 20.7ºN and 156.2ºW (Stearns, 1942; MacDonald, 1978). Its major shield-building stage, the Honomanu volcanic period, culminated ~0.95 Ma ago (Chen *et al.*, 1991). The subsequent Kula volcanic period that ended ~0.15–0.12 Ma ago (Sherrod *et al.*, 2003) built the summit to its present altitude, (~3055 m), and developed some of the cinder cones that decorate Haleakala's main crater. The most recent Hana period volcanism has produced many of the colorful cinder cones in the crater, the youngest of which are late Holocene (~8000 y). One of the youngest flows in the crater emanated from the Ka Lu'u o ka 'O'o cinder cone ~970 y ago. A combination of tholeiitic, transitional and alkalic basalts has been observed with tephra containing olivine, pyroxene, feldspar and glass (Chen and Frey, 1985; Chen *et al.*, 1991).

The compositions and mineralogy of tephra and ash at Haleakala crater, Maui, have been analyzed in order to characterize the alteration processes and products formed and to differentiate the types of alteration that are taking place at different places in the crater. Related studies of volcanic material have compared palagonitic and pedogenic alteration of tephra and ash in Iceland (Bishop *et al.*, 2002) and near Kilauea, Hawaii (Schiffman *et al.*, 2000, 2002). Solfataric alteration, or alteration in the presence of S-bearing gases, has been shown to play an important role in the alteration of volcanic material near Kilauea (Schiffman *et al.*, 2006) and may be an important soil-forming process. A previous study of altered volcanic material from Haleakala and elsewhere (Bishop *et al.*, 1998) noted mineralogical variations in samples collected at different sites at the crater. These studies have shown that there is a substantial clay fraction in the altered tephra and ash. One of the goals of the current study is to characterize the minerals in the fine (<45 μm) fractions of altered tephra and ash associated with weathering along the walls of the crater, in contrast to weathering products on or near cinder cones. Multiple analytical techniques are utilized so as to illustrate the advantages and limitations of individual methods for identification of individual minerals and phases. A significantly greater detection accuracy of these minerals and phases was achieved when combining several techniques.

* E-mail address of corresponding author:
jbishop@arc.nasa.gov
DOI: 10.1346/CCMN.2007.0550101

Basaltic material altered *via* palagonitic processes typically contains altered glass, phyllosilicates such as smectite, some Fe oxides/oxyhydroxides (FeOx), and X-ray amorphous phases (*e.g.* Schiffman *et al*., 2002). Volcanic material altered *via* pedogenic processes typically contains altered glass, phyllosilicates such as kaolinite or halloysite, goethite and other FeOx, plus organic material (*e.g.* Parfitt *et al.*, 1988). Basaltic material altered *via* solfataric processes frequently contains sulfates, silica, phyllosilicates and/or FeOx (*e.g.* Schiffman *et al.*, 2002, 2006). In some dry environments, alteration may be limited by low water activity; in such cases, altered glass and amorphous material occur as the primary phases (Morris *et al.*, 2001).

The principal reason for studying the alteration products of volcanic material from sites such as Haleakala is to characterize the pathways of alteration there. Solfataric alteration contributes to the soil-formation processes near cinder cones, while palagonitic and pedogenic alteration are more pervasive processes in the crater, although the degree of weathering, especially along crater walls, is sometimes constrained by low moisture levels. These processes also have implications for the surface of Mars where volcanic material has been exposed to substantial physical weathering and at least some aqueous activity (Carr, 1981). Evidence for phyllosillicates and sulfates in several small and isolated locations on the planet has been provided recently using the Observatoire pour la Minéralogie, l'Eau, les Glaces, et l'Activité (OMEGA) hyperspectral image cubes on Mars Express (Bibring *et al.*, 2005; Gendrin *et al.*, 2005; Poulet *et al.*, 2005). Evidence for the presence of sulfates in Meridiani Planum and Gusev crater has also been provided using Mössbauer spectroscopy, a miniature thermal emission spectrometer (Mini-TES) and other instruments on board the Mars Exploration Rovers (MERs) (Christensen *et al.*, 2004; Klingelhöfer *et al.*, 2004; Squyres *et al.*, 2004b).

METHODS

Samples

Several altered tephra pieces and some fine-grained material were collected inside the crater basin, ~1 m away from the Sliding Sands Trail and along the rim of the Ka Lu'u o ka 'O'o cinder cone. A map of Haleakala crater is shown in Figure 1, images of the collection sites are shown in Figure 2, and sample descriptions are provided in Table 1. The fine grains at all sample locations reacted to a hand-held magnet. Physical locations and colors of the samples were used to make field assignments of their type: sample 399 was thought to be an example of alteration of the dominant ash/tephra in the Haleakala crater basin, sample 397 exemplifies the alteration near cinder cones where airborne sulfuric fumes would have provided low-level, and probably long-term, solfataric alteration, sample 391 shows solfataric alteration from proximal cinder cone fumes plus additional fumes from small vents/fumeroles near the cinder cone, and samples 394–395 typify alteration in close contact with high-temperature fumes from the cinder cone.

Bulk tephra samples were gently crushed and dry sieved to 'A' <45 μm and 'B' <125 μm or 45–125 μm for further studies. The particulate samples were sent to the University of Massachusetts at Amherst and to ACME labs, Vancouver, British Columbia, for X-ray fluorescence (XRF) and inductively coupled plasma (ICP) measurements of the major elements and for C and S measurement by LECO (combustion at ~1650ºC, followed by absorption spectroscopy).

Electron microprobe analysis and scanning electron microscopy

Sieved tephra, as well as consolidated tuffs, were impregnated with epoxy resin for preparation of polished mounts for back-scattered electron (BSE) imaging and electron microprobe analysis (EMPA). Quantitative,

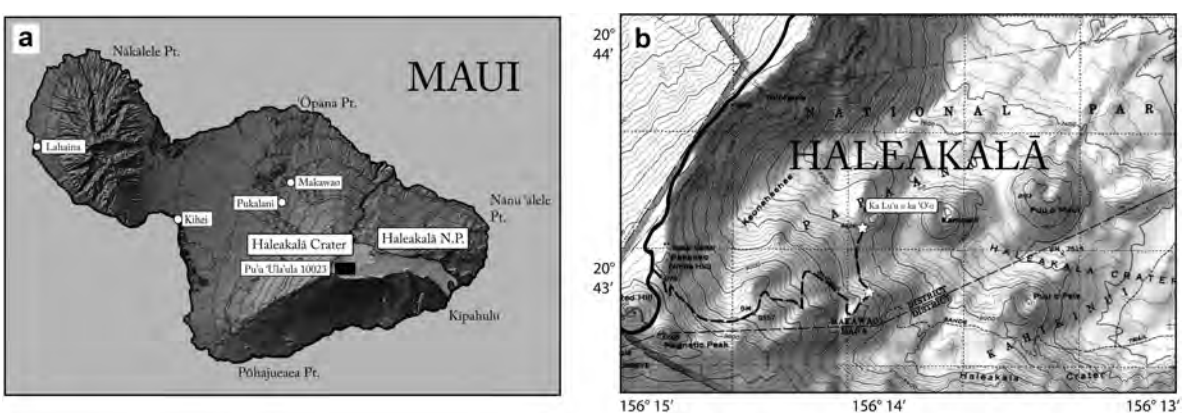

Figure 1. Map of collection sites at Haleakala crater basin, Maui: (a) view of Maui showing Haleakala National Park; (b) expanded view of Haleakala National Park showing the Sliding Sands Trail and Ka Lu'u o ka 'O'o cinder cone. Stars on the map mark the Ka Lu'u o ka 'O'o cinder cone and the trail leading to it from the Sliding Sands Trail. Samples were collected north and northwest of this cinder cone and along the Sliding Sands Trail, about 800 m down from the trailhead.

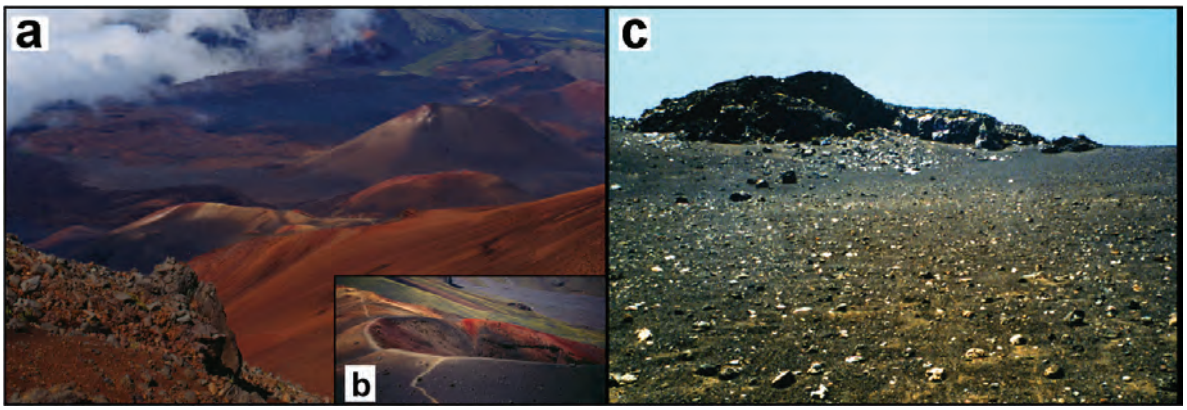

Figure 2. Images of sample collection sites at Haleakala crater basin, Maui: (a) view of cinder cones in the crater basin; (b) view of Ka Lu'u o ka 'O'o cinder cone where samples were collected (~50 m diameter); (c) view of altered tephra on the walls of the crater basin near the collection site for sample 399.

wavelength dispersive analyses by EMPA were conducted using a Cameca SX-100 microprobe operated at 15 keV, 5 or 10 nA beam current, and variable spot size. Net analyte intensities were converted to concentrations using standard ZAF correction techniques (Schiffman and Roeske, 2002).

Transmission electron microscopy

Transmission electron microscopy (TEM) was performed using a Topcon EM 002B in the Lawrence Berkeley National Laboratory. A thin-section was prepared for each sample. Copper rings were attached to selected areas and detached afterwards by gentle heating. The sample obtained was then thinned with a Fischione ion mill and carbon coated for TEM observation. The microscope was operated at 200 kV. An objective aperture of 40 μm was used as a compromise between optimum amplitude and phase contrast for images. Chemical analyses were obtained using a JEM-200CX electron microscope equipped with two Kevex EDX (energy-dispersive X-ray analysis) detectors. The microscope was operated at 200 kV (TEM or STEM mode).

X-ray diffraction

X-ray diffraction (XRD) was carried out on a Bruker D8 diffractometer equipped with a Cu tube and a diffracted-beam graphite monochromator. Samples were mixed with ethanol and precipitated on zero-background silicon slides and step-scanned from 5 to 70º2θ in 0.02º2θ increments for 45 s per increment. Selected diffraction peaks were fitted with Voigt functions using a program described by Stanjek and Friedrich (1986).

Reflectance spectra

Visible/near-infrared (VNIR) and mid-IR reflectance spectra were measured at the Reflectance Experiment Laboratory (RELAB) at Brown University. Bidirectional VNIR spectra were measured relative to Halon under ambient conditions, while biconical on-axis reflectance spectra were measured relative to a rough gold surface using a Nicolet 740 and off-axis reflectance spectra using a Nicolet Nexus FTIR spectrometer. Only small differences in the on-axis and off-axis spectra were observed and are not the focus of this study. The samples were placed in a H_2O- and CO_2-purged chamber for at least 10 h prior to measurement and during measurement in order to remove adsorbed water from the samples. Composite, absolute reflectance spectra were prepared by scaling the FTIR data to the bidirectional data near 1.2 μm. The spectral resolution is 5 nm for the bidirectional data and 2−8 cm^{-1} for the FTIR data.

Table 1. Sample descriptions.

391	basaltic ash and tephra (pieces up to ~2 cm in size), collected from the surface of a yellowish orange deposit off the path ~200 m north of Ka Lu'u o ka 'O'o cinder cone.
392	basaltic ash material, buried ~1 cm below sample 391.
394	collected from a bright red soil deposit, on the northern rim of Ka Lu'u o ka 'O'o cinder cone; reacted very strongly to a hand-held magnet, similar to sample 250 from Bishop *et al.* (1998).
395	collected just east of samples 394 and 250 along crater rim where the tephra are darker red in color.
397	basaltic ash and tephra (pieces up to ~2 cm in diameter) collected from the surface of an orange-colored deposit off the path ~100 m northwest of Ka Lu'u o ka 'O'o cinder cone.
399	collected inside the crater basin ~1 m away from the Sliding Sands Trail, far from any cinder cones or steam vents.

Emission spectra

Emission spectra were measured at the Mars Space Flight Facility at Arizona State University using a Nicolet Nexus 670 E.S.P. FTIR spectrometer. This spectrometer has been modified for emission measurements and is equipped with a thermoelectrically stabilized DTGS detector and a CsI beam splitter that allows the measurement of emitted radiation from heated samples over the mid-IR range of 2000 to 200 cm^{-1}. To reduce and maintain the amount of water and CO_2 vapor inside the spectrometer and external sample chamber and glove box (and to reduce the degradation of the hydrophilic CsI beam splitter) the entire system is continuously scrubbed using a Parker Balston compressed air and gas in-line filter.

Transmittance spectra

Transmittance spectra were obtained, using a Nicolet Magna 550 FTIR spectrometer, of samples pressed into KBr pellets prepared in order to minimize adsorption of water. 300 mg of dehydrated KBr powder were mixed with 1 mg of sample, pressed and measured against a pure KBr pellet as a background using a DTGS detector. Data were recorded from 4000 to 400 cm^{-1} at a spectral resolution of 4 cm^{-1}.

Mössbauer spectra

Mössbauer spectra were acquired at 295 and 12 K using a source of 100−90 mCi ^{57}Co in Rh on a WEB Research Co. model W100 spectrometer equipped with a Janus closed-cycle He refrigerator. Run times were 12−48 h, and the results were calibrated against α-Fe foil. The majority of the spectra were processed using the MEXDISDD program, an implementation of software described by Wivel and Mørup (1981) and written by De Grave and colleagues at the University of Ghent, Belgium. The program uses quadrupole-splitting distributions with Lorentzian lineshapes and an assumed average correlation between the isomer shift and quadrupole shift in each of two valence states. It can find a distribution for magnetic fields, rather than a single value. It calculates the full Hamiltonian and therefore is appropriate for ferrous sextets where approximations do not apply. The spectrum of sample 399 (only) was fitted using DIST3EDD, a variation of the fitting routines that is optimized for samples without magnetic phases.

Colorimetry

Quantitative color measurements were carried out by measuring the light reflected perpendicular to the dry sample surfaces over an area 8 mm in diameter using a Minolta Chroma-Meter CR-300. At least three measurements per sample were carried out using the CIE illuminant C, and data output was registered in the Munsell and CIE L*a*b* chromaticity systems. Redness ratings and fictive hematite contents were determined using the method of Barrón and Torrent (1986).

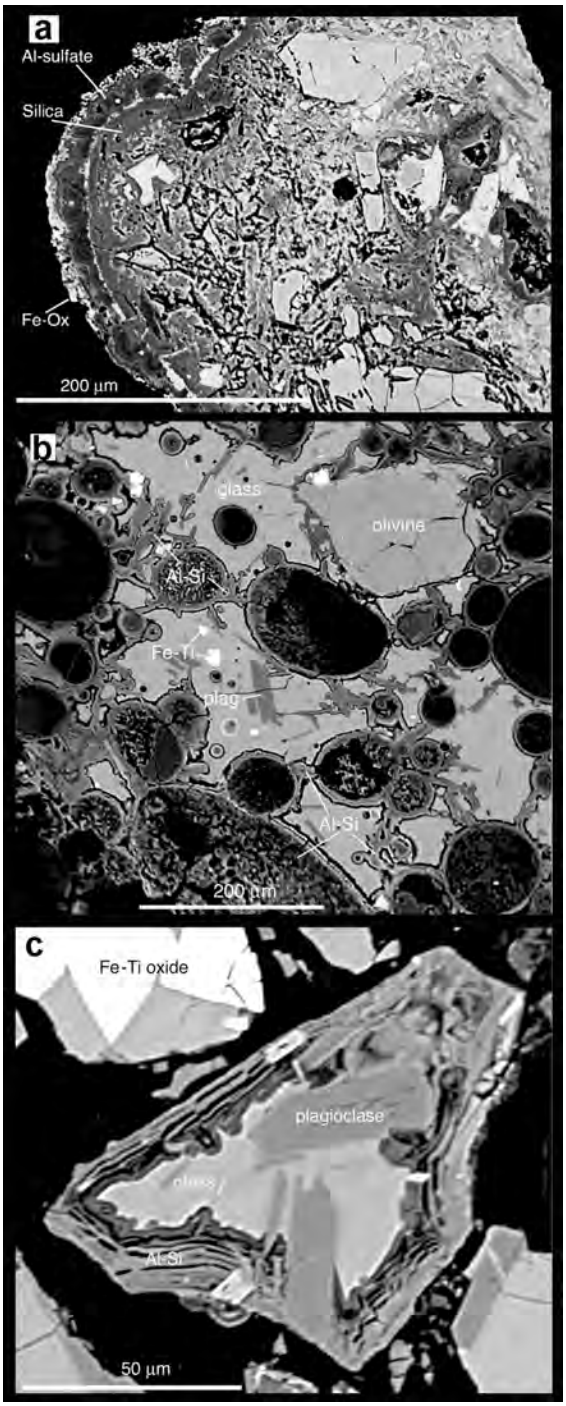

Figure 3. Back-scattered electron images of ash samples: (a) 391, (b) 397 and (c) 399. The ash contains fresh glass as well as microphenocrysts of fresh olivine, plagioclase and Fe-Ti oxides. Vesicle walls are coated, and glass-replacing veins are filled with an X-ray amorphous alumino-silicate (Al-Si). The original texture of the 391 ash fragment is preserved in the upper-right hand corner of a, although the fragment is coated with an Fe oxide or oxyhydroxide (Fe-Ox), an aluminous sulfate (Al-sulfate), and X-ray amorphous silica. A larger proportion of crystalline alteration minerals was observed in the solfataric samples 391 and 397 compared with sample 399.

RESULTS

Composition and character of tephra and altered phases

A BSE image of sample 391 is shown in Figure 3a. The original texture of the ash fragment was an intergrowth of coarse-grained olivine and Fe-Ti oxides as well as fine-grained plagioclase, pyroxene and glass (upper-right hand corner of this image). The outer few hundred micrometers of the ash particle are seen on the left side of the image and are mainly composed of concentrically zoned alteration materials: (1) a <10 μm thick discontinuous FeOx-rich outer rim; (2) a 20−30 μm thick sulfate layer; and (3) a 20−50 μm thick silica-rich layer.

The BSE image of basaltic ash 397 shown in Figure 3b displays fresh glass, as well as microphenocrysts of fresh olivine, plagioclase and Fe-Ti oxides. X-ray amorphous aluminosilicates (Al:Si molar ratio ~1:1) make up the coatings of the vesicles and replace glass in veins. The Al:Si molar ratio in the vein-filling material is closer to a smectite-like ratio of 1:2, and also contains abundant Fe and Ti. Samples 391 and 397 probably originated from the same magma based on their chemistry and location; however, the more crystalline groundmass in sample 391 compared to sample 397 suggests differences in eruption temperatures (or cooling rates). Sample 397 has also experienced less solfataric alteration in that only vesicles/veins are observed around the glass veins and no distinctive coatings and alteration rinds as in sample 391 were found here.

Figure 3c shows a BSE image of basaltic ash fragment 399 that contains fresh glass and plagioclase, and has an X-ray amorphous aluminosilicate (with Al:Si > 1:1) rind replacing the glass. The apparent concentric banding of the rind is attributed to desiccation as highly variable water contents were observed in the aluminosilicate material. This aluminosilicate also contains significant Fe and Ti, but is highly depleted in alkalis, consistent with aqueous leaching. However, only very minimal palagonitic alteration has taken place in this sample.

The major elements from bulk analyses of the altered fines are given in Table 2 and results of EMPA analyses for fresh and altered zones are presented in Table 3. These are all consistent with altered alkaline basaltic ash. The chemistry of the glass components in samples 391, 397 and 399 indicates that these ash samples were very similar when deposited. Differences in the rinds, veins and other alteration fronts are attributed to variations in their alteration histories and locations relative to the steam vents. Higher S values were measured for the samples collected near the cinder cone (2.2−4.7 wt.% SO_3) compared to sample 399 (~0.9 wt.% SO_3), which was collected near the Sliding Sands Trail far from the cinder cones. The EMPA analyses of the glass and rind of sample 399 gave even lower S abundances (<0.1 wt.% SO_3). The Mg, Ca and Na values are always lower in the altered phases, while Si, Al, Fe and Ti are sometimes elevated and sometimes reduced in the altered phases. Total C was measured at

Table 2. Bulk chemistry of dry sieved fractions of altered tephra.

	SiO_2	TiO_2	Al_2O_3	Fe_2O_3*	MnO	MgO	CaO	Na_2O	K_2O	P_2O_5	SO_3	LOI	Total
391													
(A) <45 μm	29.5	5.0	17.8	17.5	0.1	1.8	3.1	2.2	1.5	1.0	4.7	15.4	99.6
(B) 45−125 μm	39.7	4.8	14.2	14.1	0.1	3.9	6.8	2.3	1.2	0.7	n.d.	11.8′	99.8
392													
(B) 45−125 μm	37.3	4.6	15.4	13.9	0.1	3.1	5.8	2.1	1.4	0.8	4.0	10.8	99.1
250													
(A) <45 μm	27.4	2.2	11.7	38.7	0.1	1.9	4.5	1.3	1.2	0.7	3.9	5.3	99.0
394													
(A) <45 μm	18.0	1.7	10.9	48.4	0.1	1.3	2.7	1.7	0.9	0.6	4.6	9.1	99.9
(B) 45−125 μm	23.5	2.4	12.1	39.8	0.1	2.2	4.7	2.0	1.0	0.6	n.d.	9.4′	97.8
395													
(A) <45 μm	36.3	4.0	15.8	17.9	0.2	3.4	7.0	2.3	1.2	0.8	3.2	6.2	97.9
(B) 45−125 μm	40.3	3.9	15.4	15.8	0.2	4.4	8.7	2.7	1.2	0.7	n.d.	6.2′	99.5
397													
(B) 45−125 μm	38.2	4.2	15.3	17.2	0.2	3.5	5.9	1.0	0.8	0.7	2.2	9.9	99.1
399													
(A) <45 μm	32.2	4.2	21.0	16.8	0.3	2.5	5.0	1.8	0.5	0.8	0.9	13.8	99.8
(B) 45−125 μm	39.3	3.8	18.6	15.8	0.2	4.4	7.2	3.2	1.0	0.7	n.d.	5.4′	99.7

Data are given in wt.%, Fe_2O_3* is total Fe and includes both Fe^{2+} and Fe^{3+}; n.d. indicates that SO_3 was not determined for these samples and that the LOI (marked by ′) includes SO_3. The elemental abundances of the <45 μm fraction of sample 250 are similar to those reported for the <53 μm fraction of this sample reported previously (Bishop *et al*., 1998).

Table 3. Major element measurements of tephra portions from EMPA.

	SiO_2	TiO_2	Al_2O_3	FeO*	MnO	MgO	CaO	Na_2O	K_2O	P_2O_5	SO_2	Total
391												
glass	46.41	3.11	18.24	11.75	0.19	3.15	10.28	4.34	1.09	0.91	0.08	99.54
silica	72.71	6.11	3.92	3.82	0.06	0.87	0.32	0.42	0.52	0.5	2.91	92.13
sulfate	0.16	0.18	38.94	5.69	0.02	0.23	0.57	1.09	2.66	1.34	31.25	82.13
397												
vesicle Al/Si	41.7	0.25	32.63	2.59	0.06	0.84	2.54	0.24	0.23	0.99	0.19	82.25
vein Al/Si	36.22	7.48	22.69	14.9	0.18	1.02	3.08	0.18	0.26	0.74	0.14	86.89
glass	44.22	3.68	15.98	12.6	0.22	3.98	10.0	2.8	1.85	0.89	0.12	96.32
399												
glass	45.57	3.16	16.96	11.54	0.2	3.69	7.11	4.8	2.19	0.96	0.08	96.26
rind	24.29	5.48	29.89	19.35	0.04	0.07	0.7	0.21	0.04	1.16	0.0	81.21
Ave. glass	45.4	3.32	17.06	11.96	0.2	3.61	9.13	3.98	1.71	0.92	0.09	97.38

Data are given in wt.%, FeO* includes both Fe^{2+} and Fe^{3+}.

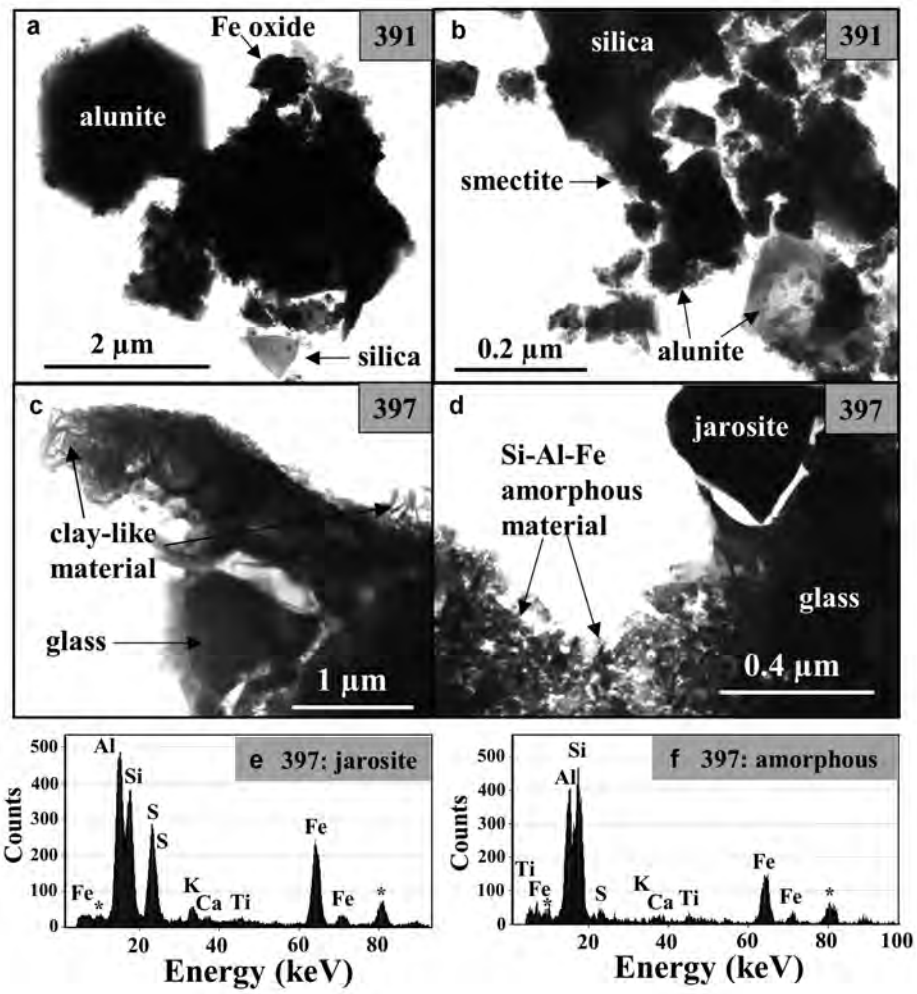

Figure 4. TEM images depicting the mineralogical composition of solfataric samples: (a) alunite, Fe oxide/oxyhydroxide and silica in sample 391; (b) silica, smectite and alunite in sample 391; (c) glass and fibrous clay-like material in sample 397; (d) glass, jarosite and SAED amorphous material in sample 397; (e) EDX data corresponding to jarosite from sample 397 shown in d; and (f) EDX data corresponding to the SAED amorphous material from sample 397 shown in d.

<0.5 wt.% for the <45 μm fractions of samples 250, 394 and 399.

Transmission electron microscopy images are shown in Figure 4a–d of the altered fractions of samples 391 and 397 that contain silica, glass, FeOx, alunite-jarosite, and selected area electron diffraction (SAED) amorphous material. Energy-dispersive X-ray plots are shown in Figure 4e,f of two regions of sample 397. Several grains of the alunite-jarosite group were observed, some with more Al and others with more Fe. The SAED amorphous material has a Si-Al-Fe composition similar to smectite minerals. For sample 391 there are also some portions that exhibit phyllosilicate-like fibrous textures. Some of the Fe oxide-bearing phases have high Ti contents, indicating that Ti-rich magnetite, ilmenite or rutile might be present. The TEM analyses of sample 399 (not shown) indicate the presence of glass, altered glass and other amorphous material with Al-Si-Ti-Fe composition in varying abundances. Some of the amorphous phases exhibit a feldspar-like composition, suggesting alteration of that mineral.

X-ray diffraction

The XRD was carried out on one or more of the <125 μm, 45–125 μm and/or <45 μm fractions of the total samples, on magnetic separates of the <125 μm or 45–125 μm fractions, and on selected samples from which magnetic fractions had been extracted using a hand magnet. Many of these are shown in Figure 5. All samples exhibit complex mineralogy including plagioclase, pyroxene, Na-alunite, Na-jarosite, hematite and magnetite in proportions ranging from dominant to barely detectable. Most samples also contain some glass, indicated by a broad background centered near a *d* value of ~0.35 nm. An additional minor bulge at a *d* value of ~0.40 nm in the background of two samples

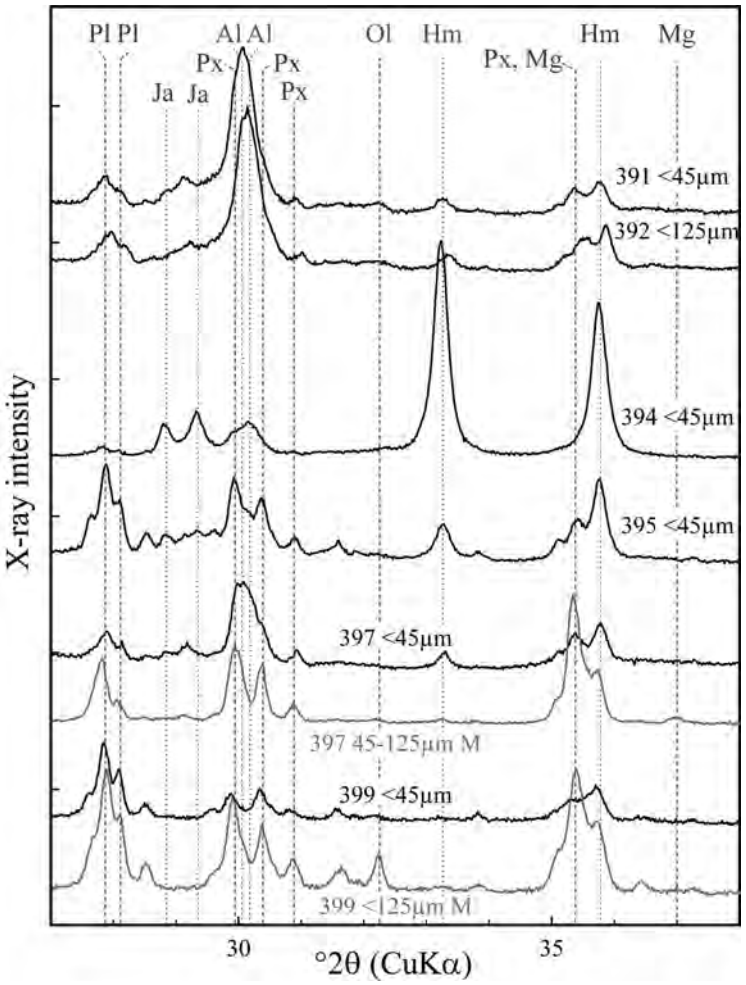

Figure 5. XRD traces of the Haleakala samples with characteristic peaks marked for mineral identification: plagioclase (Pl), pyroxene (Px), olivine (Ol), magnetite (Mg), Na-jarosite (Ja), Na-alunite (Al) and hematite (Hm). The positions of primary mineral peaks are indicated with broken lines, whereas those of secondary minerals are indicated with dotted lines. XRD data of the magnetic separates (M) from samples 397 and 399 are shown in lighter shades. The vertical axes are scaled such that the tick marks correspond to 100 counts/s.

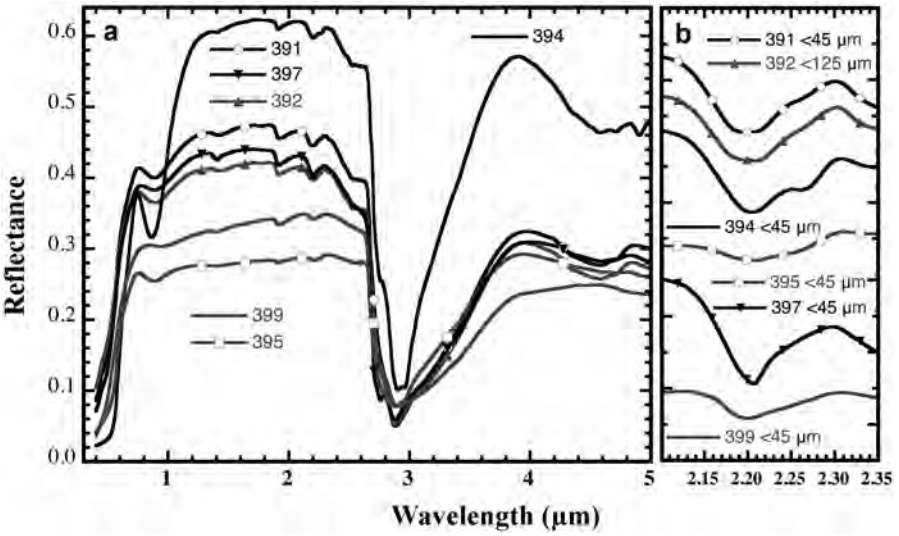

Figure 6. VNIR reflectance spectra of fines: (a) 0.3 to 5 μm; (b) relative reflectance of OH combination band region.

(391 and 392) suggests the possible presence of opal, and one sample (397) contains a phyllosilicate. As the feldspar and pyroxene may vary widely in chemical composition and even crystallographic symmetry, definitive mineral identification is difficult due to the presence of multiple constituents in these samples.

The XRD indicated Na-alunite and, to a lesser extent, plagioclase to be the principal constituents of samples 391 and 392; the mineralogy of 394 is dominated by hematite, a less marked content of Na-jarosite, and lack of glass, while a relatively intense peak at 0.251 nm in the magnetic extract of this sample points to the presence of a maghemite 313 peak in addition to remnant hematite (whereas no magnetite could be observed); 395 also contains significant proportions of hematite and plagioclase, whereas the mineralogies of 397 and 399 are dominated by plagioclase. Sample 394 differs from the other samples in that it contains significantly less (possibly even no) glass, and sample 399 differs from the others in that no alunite, jarosite or hematite could be detected by XRD. It is also the only sample in which peaks that can be attributed to olivine were observed.

Quantification of magnetite and maghemite in the magnetic separates is challenging because of parallel extraction of other minerals. However, a comparison of XRD data for the bulk samples and the magnetic separates indicates a significant proportion of magnetite in sample 397. An unequivocal identification of maghemite proved impossible because of multiple mutual interferences from other minerals. Even in the magnetic separates, the principal maghemite peaks (313 and 220) are difficult to use for identification of this mineral because of interferences from peaks of concurrently extracted pyroxene (present in all magnetic samples) or remnant hematite. This coexistence of pyroxene with magnetic minerals indicates that the latter formed at least in part by exsolution from pyroxenes that had originally been rich(er) in Fe.

VNIR spectroscopy

In Figure 6, visible/near-infrared (VNIR) spectra are shown of the <45 μm fractions, and of multiple grain-size fractions in Figure 7. The VNIR spectra of all samples are dominated by a strong band near 3 μm attributed to water bound in glass and X-ray amorphous phases as these spectra were measured under controlled dehydrated conditions where the adsorbed water was very low. In the spectrum of sample 399, this is a broad

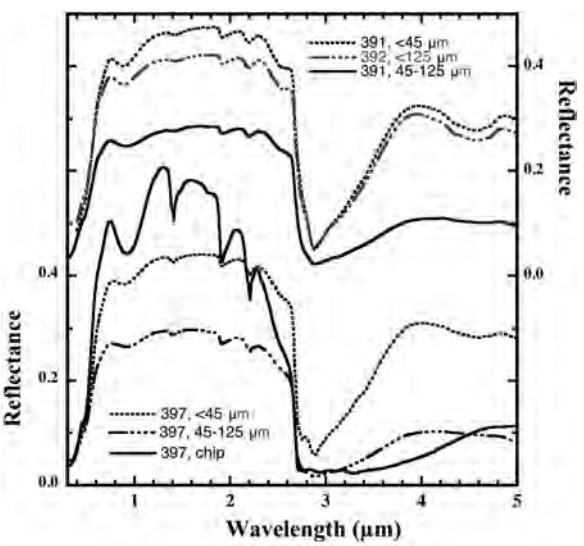

Figure 7. VNIR reflectance spectra of multiple grain sizes of samples 391 and 397. Both on-axis and off-axis reflectance spectra were measured in the IR region for the coarser-grained (45–125 μm) samples and only minor differences were observed.

rounded feature, centered near 2.9 μm, which is characteristic of adsorbed water or water in glass. Spectra of samples 394 and 395 exhibit a shoulder near 2.75 μm (attributed to Al-OH in montmorillonite and other phyllosilicates, *e.g.* Bishop *et al.*, 1994), and a doublet at 2.90 and 2.97 μm (consistent with alunite and jarosite, *e.g.* Bishop and Murad, 2005). Spectra of samples 391 and 397 are consistent with alunite, and an Al-bearing phyllosilicate plus alunite, respectively, due to features at 2.75 and 2.89 μm. Spectra of samples 391, 394 and 397 are compared with lab reference spectra of alunite and jarosite in Figure 8. Structural OH (rather than bound water) is spectrally dominant in the spectrum of sample 394. A broad shoulder near 2.9–3.2 μm in spectra of samples 391, 395 and 397 is consistent with some bound water – probably in X-ray amorphous aluminosilicate phases.

All spectra also exhibit an Fe band near 0.9–1.0 μm and hydration features near 1.4, 1.9 and 2.2–2.3 μm that vary in intensity and spectral character. The extended visible region band centers occur near 0.89 μm for samples 391, 392, 395, 397, near 0.87 μm for sample 394, and near 0.93 μm for sample 399. The extended visible region spectra of samples 391, 394 and 399 are compared with spectra of selected Fe oxide/oxyhydroxide minerals in Figure 9. Due to the weak, broad band observed here for many samples, the Fe-bearing components probably include nanophase, poorly crystalline and/or amorphous phases. The spectrum of sample 394 is clearly dominated by hematite, although other Fe-bearing phases such as jarosite, maghemite and ferrihydrite may also be contributing to this spectrum. The 399 spectrum is consistent with both poorly crystalline and/or X-ray amorphous Fe^{3+} phases plus Fe^{2+}-bearing species. The Fe bands in this region tend to be shifted towards longer wavelengths for spectra of the coarser size fractions, indicating that Fe^{2+} components may be present in the >45 μm fractions of these samples.

The feature near 1.4 μm is due to both OH and water, while the band near 1.9 μm is due only to H_2O. These features are typical of smectites and other phyllosilicates and are also observed for hydrated silica (*e.g.* Bishop *et al.*, 2004). These bands are very weak and broad for the spectra of <45 μm Haleakala samples. As shown in Figure 7, these bands are much stronger for the spectrum of the sample 397 tephra chip. This spectrum exhibits a doublet at 1.38 (Si-OH) and 1.41 (Al-OH) μm with a shoulder at longer wavelengths due to the water overtone vibration.

The spectra of samples 391–392 in Figure 6b exhibit a band from 2.18 to 2.21 μm that is broader than typically observed for the Al-OH combination band in either alunite (2.17 μm) or montmorillonite (2.20–2.21 μm), plus weak shoulders that are character-

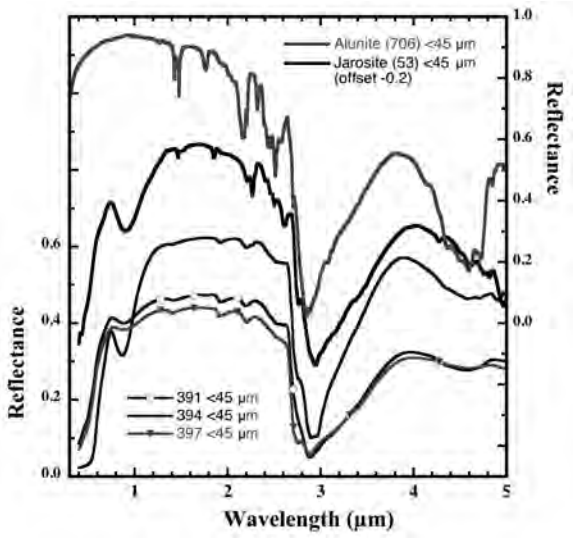

Figure 8. VNIR reflectance spectra of samples 391 and 397 compared with spectra of reference minerals jarosite and alunite. The spectra of samples 391 and 397 have well developed broad alunite-like bands centered near 4.5 μm, while the spectrum of sample 394 has some alunite-like character near 4.5 μm overlain by jarosite-like features near 4.6, 4.8 and 4.9 μm. The spectra of samples 391 and 397 also exhibit weak bands near 1.77 μm that are characteristic of alunite. This band is somewhat enhanced in the 397 chip spectrum in Figure 7.

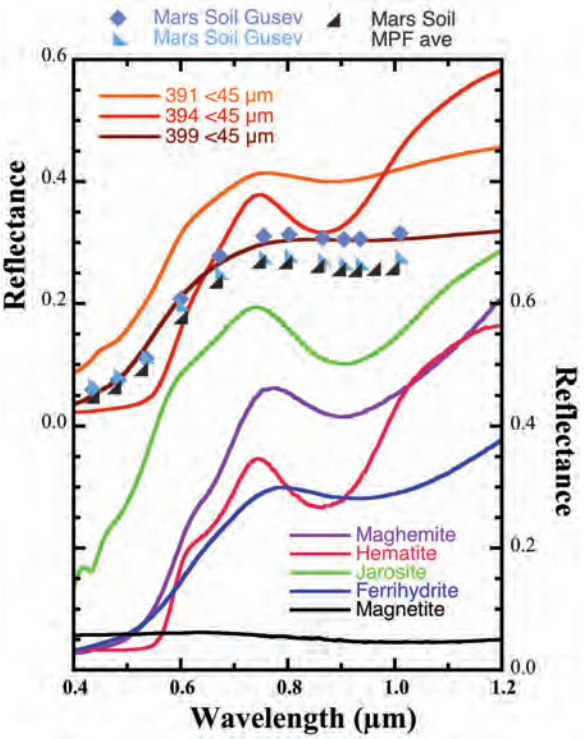

Figure 9. Extended visible region spectra of samples 391, 394 and 399, along with spectra of several Fe oxide/oxyhydroxide minerals for comparison. Multi-channel Mars spectra of Gusev soil (Bell *et al.*, 2004) and Mars Pathfinder soil (Smith *et al.*, 1997) are also given.

istic of the Fe-OH combination band in jarosite (2.27 μm) spectra. The spectrum of sample 394 has a well-defined band at 2.21 μm, a strong shoulder at ~2.27 μm, and a weak inflection near 2.17 μm that is consistent with the presence of montmorillonite, jarosite and perhaps alunite in that order. The 395 spectrum exhibits weaker features near 2.205 and 2.27 μm, indicative of montmorillonite and jarosite. The 397 spectrum has a sharp band at 2.208 μm and a shoulder at longer wavelengths consistent with Fe-OH species. The 399 spectrum has a broad feature consistent with mostly Al-OH and some Fe-OH species in a poorly crystalline matrix. The presence of OH-bearing sulfates such as jarosite and alunite can be distinguished from phyllosilicates by the sulfate bands near 1.7−1.85 and 4−5 μm.

Mössbauer spectroscopy

The complex mineralogy of the Haleakala samples combined with the high Fe contents of the original lavas leads to intricate Mössbauer spectra comprising multiple doublets and sextets that are difficult to fit and interpret (Table 4). Due to the complexity and overlapping nature

Table 4. Mössbauer parameters.

Sample	*T* (K)	Phase assigned	δ (mm/s)	Δ (mm/s)	γ (mm/s)	Field (Tesla)	%
JB391-A	293	hematite	0.37	−0.25	0.40	51.9	21
		jarosite	0.36	1.26	0.38		26
		Fe^{3+}	0.35	0.67	0.48		13
		Fe^{2+} silicate	1.03	2.35	0.76		39
	12	hematite	0.48	−0.14	0.40	53.3	20
		hematite	0.47	−0.15	0.46	50.1	9
		hematite	0.49	−0.19	0.56	47.0	26
		jarosite	0.46	1.12	0.76		26
		Fe^{2+} silicate	1.28	2.72	1.27		19
JB392	293	hematite	0.37	−0.23	0.38	51.2	22
		jarosite	0.35	1.24	0.43		24
		Fe^{3+}	0.33	0.66	0.60		36
		Fe^{2+} silicate	1.11	2.54	0.54		8
		Fe^{2+} silicate	1.05	1.91	0.49		9
	12	hematite	0.47	−0.13	0.58	53.0	27
		hematite	0.46	−0.14	0.46	49.0	19
		jarosite	0.43	1.19	0.47		14
		Fe^{2+} silicate	1.26	2.50	1.34		31
		Fe^{3+} silicate	0.17	0.35	0.59		8
JB395-A	293	hematite	0.36	−0.21	0.43	51.0	35
		jarosite	0.36	1.25	0.41		17
		Fe^{3+}	0.35	0.72	0.63		29
		Fe^{2+} silicate	1.05	2.23	0.85		20
JB397-A	293	hematite	0.35	−0.22	0.33	51.3	21
		jarosite	0.36	1.19	0.39		17
		Fe^{3+}	0.36	0.67	0.51		43
		Fe^{2+} silicate	1.04	2.27	1.03		19
JB399-A	293	jarosite−alunite	0.33	1.12	0.60		38
		Fe^{3+}	0.32	0.54	0.30		42
		Fe^{2+} silicate (Px)	1.12	1.84	0.49		10
		Fe^{2+} silicate (Px)	1.12	2.16	0.30		4
		Fe^{2+} silicate (Ol)	1.13	3.02	0.30		6
JB394-A	293	hematite	0.36	−0.22	0.35	51.1	82
		jarosite	0.36	1.16	0.45		14
		Fe^{3+} silicate	0.16	0.46	0.93		4
	12	hematite	0.47	−0.11	0.40	53.8	83
		hematite	0.50	−0.04	0.30	48.2	9
		jarosite	0.43	1.50	0.80		6
		Fe^{3+} silicate	0.15	0.44	0.50		1

'Jarosite' refers to any composition along the alunite-jarosite solid solution; 'Fe^{3+}' refers to a paramagnetic Fe^{3+} component or a superparamagnetic Fe oxide; 'Fe^{2+} silicate' refers to Fe^{2+} in silicate minerals or glasses; 'Px' refers to pyroxene and 'Ol' refers to olivine.

of these spectra, errors in isomer shift and quadrupole splitting are unusually high, probably ±0.05–0.10 mm/s, and errors in the hyperfine fields are at least ±0.15 T. With the exception of the spectrum of sample 394, the room-temperature spectra are dominated by Fe^{3+} doublets that may result from either genuinely paramagnetic minerals or glasses, or oxides that, because of small particle size, are subject to superparamagnetic relaxation (Murad and Johnston, 1987). Magnetically ordered components with hyperfine fields >51 T at room temperature that are dominant in sample 394, subordinate in samples 391, 392, 395 and 397, but absent in sample 399, can be unequivocally attributed to hematite. Figure 10 shows spectra of selected Haleakala samples and of two soils taken by the Mössbauer spectrometers on the Mars rovers for comparison. The lines of these magnetic components of the Haleakala samples are asymmetrically broadened towards lower hyperfine fields, indicating either poorly-crystalline oxides (*e.g.* Murad and Johnston, 1987; Morris *et al.*, 1989) or admixtures of a low hyperfine field mineral such as maghemite. Subordinate Fe^{2+} doublets are attributed to unweathered remnants of the original pyroxene and olivine. Because we used unconstrained fits (peak positions, widths and areas were allowed to vary freely), the results often yielded parameters that were difficult to assign to a specific mineral (Table 4).

In contrast to the room-temperature spectra, spectra taken at 12 K (Figure 11) display multiple magnetically ordered constituents in addition to the paramagnetic components, enabling better resolution of these components at lower temperature than at 293 K and producing slight variations in the component percentages. Furthermore, poorly-crystallized Fe oxides and oxyhydroxides tend to have distributions of magnetic hyperfine fields rather than unique well-defined fields (*e.g.* Murad and Johnston, 1987; Morris *et al.*, 1989); such distributions required multiple hematite components in our spectra (Table 4). So, although we acquired both 293 and 12 K spectra of all samples in this study, we were able to obtain useful fits to 12 K spectra only for samples 391, 392 and 394. Fortuitously, in the other cases, the oxide components were sufficiently well resolved at 293 K that interpretations could be made.

Comparison of Mössbauer results for samples 391, 392 and 394 (Figure 11) shows that the amount of Fe^{2+} is greatest in 392, which was underneath 391 and thus experienced less surface weathering. Sample 391 has more Fe^{3+}, suggestive of alteration of tephra and ash particles to more oxidized phases. Sample 394 contains no Fe^{2+} and the Fe mineralogy is dominated by hematite.

The Mössbauer spectrum of sample 399 was the only one in which a contribution from olivine could be resolved, which is consistent with the XRD analyses. In 395 and 397, there is also a well-defined doublet with parameters of ~1.04 mm/s for isomer shift (IS) and ~2.25 mm/s for quadrupole splitting (QS). Based on the TEM and XRD results and through analogy with previous Mössbauer studies of pyroxene, this doublet probably represents Fe^{2+} in pyroxene.

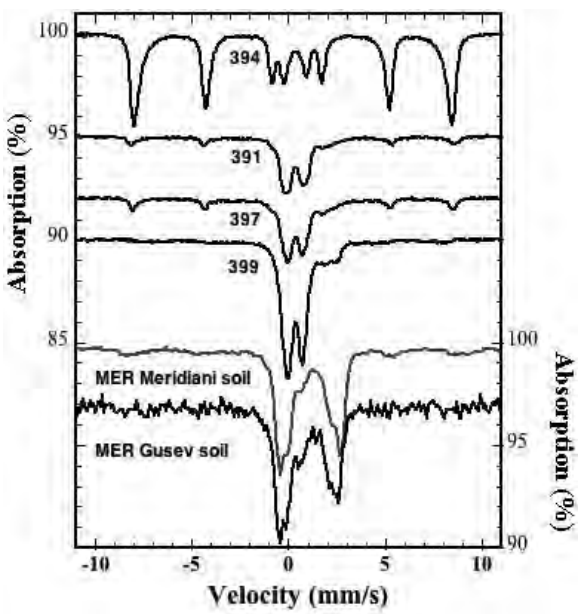

Figure 10. Room-temperature Mössbauer spectra of samples 391, 394, 397 and 399, compared with spectra of Martian soil from Meridiani Planum and Gusev crater. The Martian spectra have been processed and calibrated using the *MERView* software package described by Agresti *et al.* (2006); data are available at http://www.mtholyoke.edu/go/mars/.

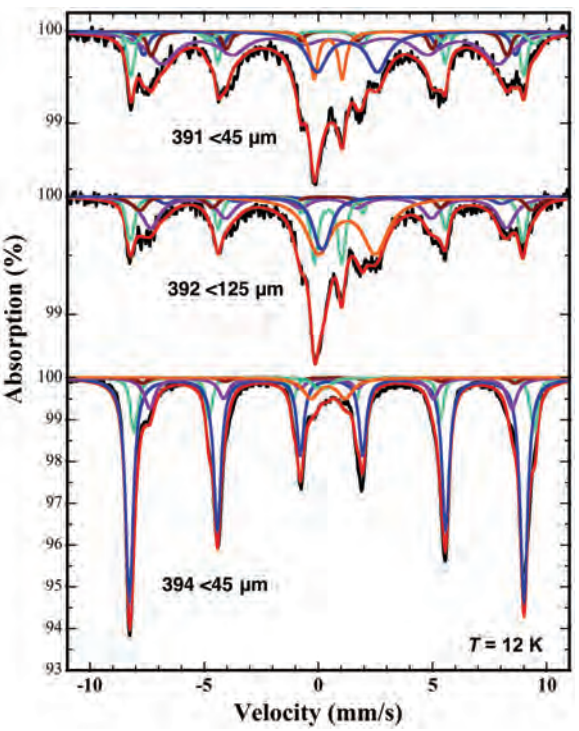

Figure 11. Low-temperature Mössbauer spectra of samples 391, 392 and 394.

Nearly all of the spectra contained doublets corresponding to Fe^{3+} in different types of octahedral sites: one with IS ~0.33 mm/s and QS = 1.15 mm/s, and a second doublet with IS = 0.36 mm/s and QS ~0.70 mm/s. We assign these doublets to jarosite, though we note that the second doublet could also be assigned to ferrihydrite (which was not seen in the XRD results). We note that there are many other silicates, oxides and sulfates with similar parameters, and stress that mineral identifications here are facilitated by corroborating data from other methods.

Color measurements

Because of the strong pigmenting power of hematite, soil colors determined using the CIE L*a*b* system, recalculated to give a 'redness rating', can give an indication of the hematite contents of soils and synthetic hematite/goethite/soil mixtures (Barrón and Torrent, 1986). Color measurements on the samples studied here – with the exception of sample 399 – confirm this, indicating hematite contents to decrease in the order 394 >> 395 >> 391 ~ 392 ~ 397, in agreement with the Munsell hues and the relative hematite contents indicated by XRD (Table 5). The failure of this relation to explain the color of sample 399 probably arises because this sample is relatively fresh, and the primary minerals are determining the colors rather than secondary Fe oxides.

Mid-IR spectroscopy

Mid-IR reflectance and transmittance spectra of samples 391, 392, 394 (and 250), 395, 397 and 399 are shown in Figure 12. In many cases for fine-grained materials in this spectral region, the transmittance spectra provide more spectral character than reflectance and emission spectra. A water-bending vibration is observed in all spectra near 1630–1640 cm^{-1} (~6.1 μm). Additional features are observed near 1000–1200 cm^{-1} (~8–10 μm) and 450–600 cm^{-1} (~17–22 μm) that are primarily due to silicate, sulfate and oxide vibrations in minerals (Farmer, 1974; Salisbury *et al.*, 1991). Some differences are observed here with particle size, due in part to a larger fraction of

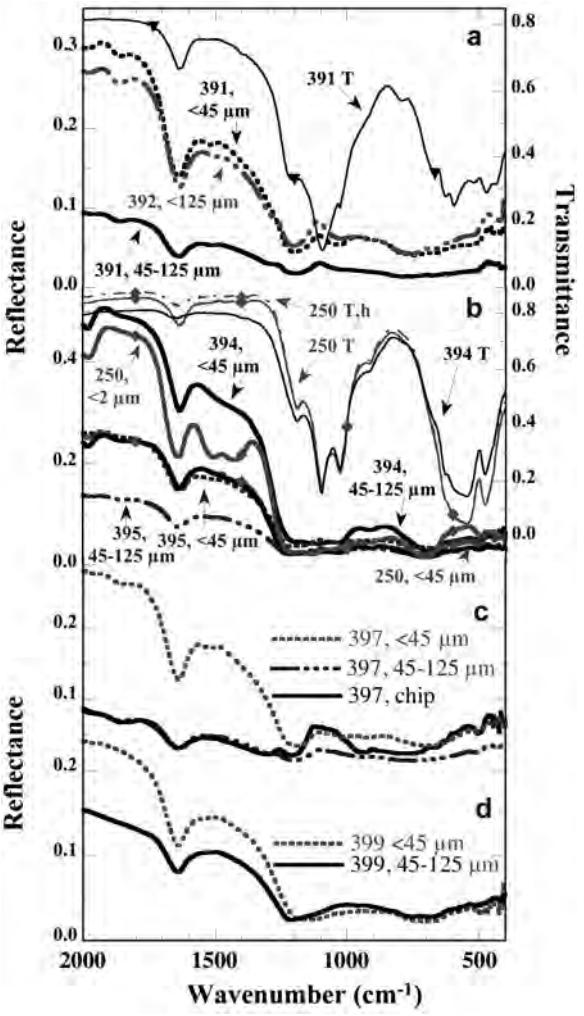

Figure 12. Mid-IR reflectance and transmittance spectra: (a) reflectance spectra of samples 391 and 392 compared to transmittance spectra of sample 391; (b) reflectance spectra of samples 250, 394 and 395 compared with transmittance spectra of 250 and 394 (sample 250 was re-measured after heating for 49 h at 100ºC and is marked with an h); (c) reflectance spectra of three size fractions of 397; and (d) reflectance spectra of two size fractions of 399.

Table 5. Colors of altered Haleakala tephra fractions.

Sample	Munsell		L*	a*	b*	RR	Hm %[1]	Hm_{104}[2]
JB391 <45 μm	7.2 YR	6.0/3.2	60.54	7.22	18.87	1.48	0.75	6
JB392 <125 μm	6.8 YR	5.8/2.6	58.48	6.35	15.17	1.61	0.81	7
JB394 <45 μm	9.3 R	4.5/5.7	45.63	22.78	19.17	26.01	11.19	100
JB395 <45 μm	3.1 YR	4.8/3.4	49.33	11.78	15.93	8.36	3.68	16
JB397 <45 μm	7.8 YR	5.6/3.1	57.02	6.47	18.17	1.90	0.93	7
JB397 45–125 μm	8.9 YR	5.3/2.3	54.06	4.13	14.16	1.67	0.83	5
JB399 <45 μm	8.6 YR	5.2/3.1	52.69	5.80	18.81	2.73	1.29	1[3]

[1] Redness ratings and fictive hematite contents after Barrón and Torrent (1986); [2] relative intensity from fitted XRD 104 peak; [3] not significant ($<\sqrt{(3 \times \text{background})}$).

alteration minerals in the finer fractions. Coarse particles also exhibit stronger fundamental features in this region due to increased surface scattering compared to the dominance of volume scattering in fine-grained samples (*e.g.* Salisbury and Wald, 1992) as seen in the stronger Reststrahlen band near 1100 cm^{-1} for the 397 chip spectrum compared to the 397 powder spectra.

Figure 13 shows transmittance spectra of samples 391 and 394 (plus 250) compared with spectra of several minerals. The spectra of samples 394 and 250 are very similar and exhibit a strong triplet at 1026, 1096 and 1188 cm^{-1}, plus a shoulder near 628 cm^{-1}, attributed to jarosite, and a strong doublet at 487 and 545−590 cm^{-1}, attributed to hematite. Phyllosilicates and/or X-ray amorphous Al-Si-Fe are also likely to be present with a broad Si−O stretching band near 1000−1100 cm^{-1} and an Al-OH bending vibration at 912 cm^{-1}. Jarosite and montmorillonite both have features near 500 cm^{-1} that would be consistent with the 394 and 250 spectra; maghemite, magnetite, and alunite could also be contributing to features in this region. The spectrum of sample 391 exhibits a strong band at 1092 cm^{-1} and additional features at 443, 593, 625, 665, 1026, 1092 and 1200 cm^{-1} that are consistent with alunite. The band at 468 cm^{-1} is consistent with montmorillonite and the band near 790 cm^{-1} may be due to an X-ray amorphous Si-OH phase.

Emission spectra of fine-grained fractions and tephra chips of the Haleakala samples are shown in Figure 14; all show water bands near 1640 cm^{-1}. Some also show additional features in the ~1400−1500 cm^{-1} range. A related doublet has also been observed for ferrihydrite collected in Iceland (Bishop and Murad, 2002), selected hydrated iron sulfates (Lane *et al.*, 2004), and neutralized acid mine drainage material (Bishop *et al.*, 2005). Detailed analyses of this feature for hydrated iron sulfates suggests that this doublet is due to a splitting of the water bending vibration in some minerals (Lane, 2007). At longer wavelengths the emissivity is close to 1 with some weak features.

Summary of alteration phases formed

Table 6 presents a summary of minerals and phases detected by our integrated analytical studies of the Haleakala tephra samples. The EMPA/SEM analyses coupled with bulk major element analyses of the tephra fragments of samples 391 and 397 indicate that these are altered alkaline basalt. The tephra fragments include fresh glass, olivine, pyroxene, plagioclase and Fe-Ti oxides. The thickness and abundance of coatings and alteration rinds indicates that sample 391 experienced greater alteration than sample 397. Samples 391 and 397 were collected near the Ka Lu'u o ka 'O'o cinder cone and experienced solfataric alteration. Transmission electron microscopy of the altered phases of 391 and

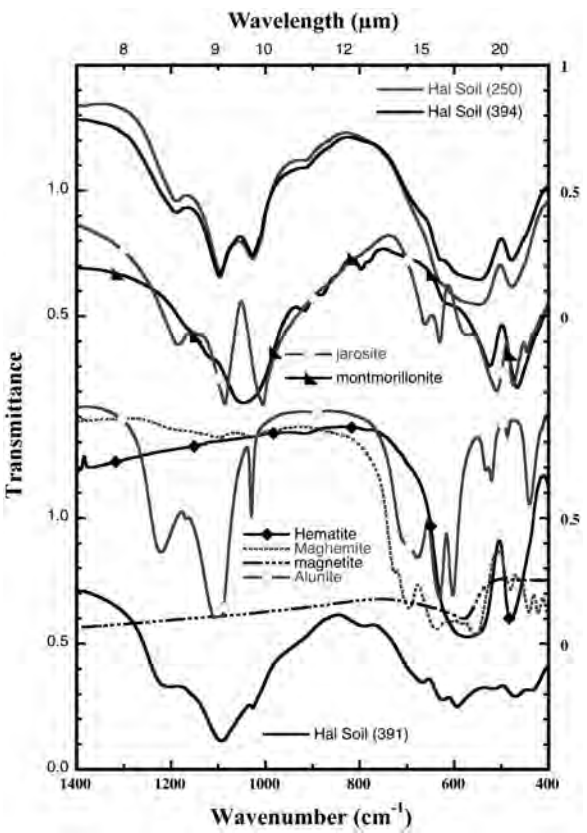

Figure 13. Transmittance spectra of samples 391 and 394 (plus 250) are compared with spectra of the minerals jarosite, montmorillonite, hematite, maghemite, magnetite and alunite. All samples and minerals were dry sieved to <45 μm particle size.

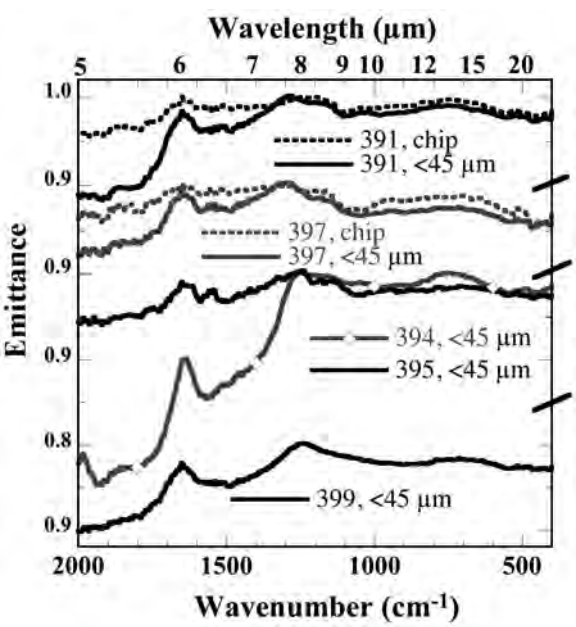

Figure 14. Emission spectra of the fine-grained fractions of samples 391, 394, 395, 397 and 399, plus spectra of tephra chips of samples 391 and 397.

Table 6. Composition summary of altered fines from all techniques.

Sample	Plagioclase feldspar	Pyroxene	Olivine	Glass	Magnetite	Maghemite	Hematite	Na-Alunite	Na-Jarosite	Phyllosilicate	Amorphous Al/Si material
391	++			+	+		+	++	+	+	+
392	++			+	+		+	++	+		+
394	+					?	++	+	++	+	
395	++			+	+		++	+	+		+
397	++			+	+		+	+	+	+	+
399	++	+	+	+	+						

+++ dominant, ++ abundant, + minor

397 showed glass, altered glass, Fe oxides/oxyhydroxides, and X-ray amorphous material. The presence of some X-ray amorphous or nanophase Fe oxides/oxyhydroxides is supported by TEM and extended visible region spectra, but was not sufficiently abundant to be detected by XRD. Some phyllosilicate texture was observed in TEM of sample 391 and phyllosilicate features were observed in IR spectra of sample 391, while XRD only showed evidence of a phyllosilicate in sample 397. Na-alunite and jarosite were observed in XRD of all samples except 399, which is consistent with the IR spectra; Mössbauer spectra showed the presence of alunite/jarosite in all samples. Alunite-jarosite grains were observed by TEM analyses of both 391 and 397 and it is likely that these have formed as something like a solid series with some Al-dominated and some Fe-dominated samples. Sample 392 was collected underneath sample 391 and has a similar composition with less extensive alteration.

Sample 399 was collected far from any cinder cones and represents a more typical alteration environment for the Haleakala crater. The XRD and Mössbauer spectroscopy showed the presence of pyroxene and olivine in sample 399, which is consistent with the VNIR spectra showing more Fe^{2+} material in this sample compared to the others. The TEM of the altered fraction of 399 showed glass, altered glass, other amorphous material and Fe oxides/oxyhydroxides. The IR spectra of this sample showed the strongest bound water features and weakest OH features.

Sample 394 is the most highly altered and is similar to sample 250 collected earlier. Both were collected on the rim of the Ka Lu'u o ka 'O'o cinder cone at the brightest red region. Samples 394 and 250 exhibit the strongest response to a magnet and are dominated by hematite, magnetite, Na-jarosite and an Al-phyllosilicate. In contrast to the others, sample 394 did not show evidence of glass by XRD. It appears that samples 394 and 250 were altered directly by the steam emanating from the cinder cone that completely removed the glass and primary minerals. Sample 395 is similar, but also contains some X-ray amorphous Al-Si material and altered glass. Sample 395 was collected just east of this area and probably experienced significant alteration from steam, but this sample was not as completely altered as samples 394 and 250.

APPLICATIONS TO MARS

The Mars Exploration Rovers (MERs) have on board a Mössbauer spectrometer, a multi-channel panoramic camera (PANCAM) and a miniature thermal emission spectrometer (Mini-TES) that are providing mineralogical information on the surface of Mars (Squyres *et al.*, 2004a). Figure 9 contains PANCAM multi-channel spectra of soil from Gusev crater (Bell *et al.*, 2004), along with an average soil spectrum from Mars Pathfinder (Smith *et*

al., 1997). These Martian soil spectra are very similar to the Haleakala sample 399 spectrum.

Figure 10 shows our results compared with Mössbauer spectra of Martian soil from the Meridiani (Klingelhöfer *et al.*, 2004) and Gusev (Morris *et al.*, 2006) regions. Our data, which have twice the resolution of the MER results, and were acquired using long run times, optimal laboratory conditions and thin absorber geometry, proved extremely difficult to interpret because of the presence of multiple, strongly overlapping peaks from oxide sextets. Based on this experience, it is likely that unequivocal identification of specific Fe oxides in the MER data will be problematic. However, Mössbauer spectra in our study, and in Martian data, contribute greatly towards mineral characterization by providing the relative abundance of Fe^{2+} to Fe^{3+} components and by enabling identification of some specific minerals and/or mineral groups such as pyroxene, olivine, magnetite, hematite, other FeOx minerals, and jarosite-like ferric sulfates.

An emissivity doublet initially attributed to carbonates (Bandfield *et al.*, 2003) has been identified in TES data of Martian dust material near 1380 and 1580 cm^{-1} (or ~6.3 and 7.2 μm). Similar features have been observed for the fine-grained Martian surface material by the Mini-TES spectrometer on the MERs (Christensen *et al.*, 2004). These spectra are compared to mid-IR spectra of selected Haleakala samples in Figure 15. Spectra of the <45 μm fractions of samples 394 and 250 contain a broad band spanning this range and spectra of the <2 μm fraction of sample 250 exhibits a doublet very similar to that observed in the TES and Mini-TES spectra of Martian fines. Because carbonates were not detected by any technique in this study, they do not need to be invoked to explain these features, which are in this case produced by altered volcanic tephra. We attribute this doublet to a splitting of the water deformation band observed in some hydrated Fe oxides and sulfates (Lane, 2007).

SUMMARY AND IMPLICATIONS

The altered fractions of basaltic tephra from the crater wall, the rim of a cinder cone and near a cinder cone in Haleakala, Maui, have been characterized using multiple techniques. A number of alteration products have been observed including Fe oxides/oxyhydroxides, phyllosilicates and sulfates. The samples collected on the crater rim are extremely altered and contain the largest abundance of Fe oxides/oxyhydroxides, some jarosite, and a minimum of glass and silica phases. The samples collected near the cinder cone contain altered glass, X-ray amorphous material, Fe oxides/oxyhydroxides, alunite, and in some cases a montmorillonite-like phyllosilicate.

Mössbauer spectra of these samples provided definitive Fe^{2+}/Fe^{3+} information about the samples and could be combined with other data in many cases to make assignments of the Fe mineralogy. This is similar to Mössbauer results for the complex fines covering the surface of Mars, where Fe^{2+}/Fe^{3+} results can be definitively assigned, but mineralogical assignments must be made in conjunction with other techniques. Greater Fe^{2+}/Fe^{3+} ratios were observed for the Martian fines than the Haleakala fines, suggesting that the Martian fines are less altered (*i.e.* less oxidized).

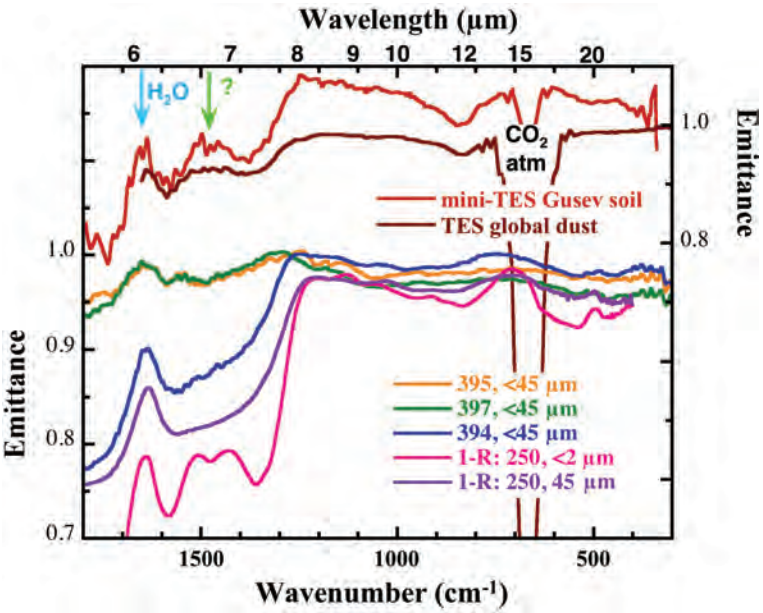

Figure 15. Emission spectra and converted reflectance spectra (E=1−R) of selected fine-grained samples compared to TES (Bandfield *et al*., 2003) and Mini-TES (Christensen *et al*., 2004) spectra of Martian fines.

Specific sulfate minerals such as alunite and jarosite were identified in the VNIR spectra and could be identified on Mars as well using OMEGA or CRISM hyperspectral images. The presence of OH-bearing minerals such as phyllosilicates was also indicated, but specific mineral assignments were difficult. Variations in the water bands near 1.9 and 3 μm can be used to detect hydrated components as in a recent study by Milliken and Mustard (2005).

In the mid-IR region the transmittance spectra were best for identification of small amounts of alteration minerals; however, differences in spectral character near 500 and 1000 cm^{-1} (10 and 20 μm) are significant enough to differentiate these samples using the emissivity data from TES or Mini-TES. The spectral character of the Haleakala samples near 1300–1650 cm^{-1} contains a water band plus additional features for some highly altered samples that may have implications for Mars as well. The doublet observed here is not yet well understood, but is probably due to water deformation modes in some combination of Fe oxides/oxyhydroxides, jarosite/alunite, and/or phyllosilicate, all of which are present in these samples. Further study of these features may help explain the enigmatic doublet observed here in the TES and Mini-TES data of Martian fines.

ACKNOWLEDGMENTS

The authors wish to thank R. Nagata of Haleakala National Park for providing information about the crater and the trails, T. Hiroi for assistance with the bidirectional spectra, E. Sklute for assiatance fitting the Mössbauer data, L. Gründler for assistance with sample collection, L. Ly for assistance with the maps, and to M. Schaefer, P. Heaney and an anonymous reviewer for comments that improved the text. Samples were collected with permit # HALE-2004-SCI-0005. Funding for this project was provided by NASA's MFR program. RELAB is a multi-user facility at Brown University supported by NASA grant NAG5-3871. MDD acknowledges support from NASA grant NNG04GG12G.

REFERENCES

Agresti, D.G., Dyar, M.D. and Schaefer, M.W. (2006) Derivation of velocity scales for Mars Mössbauer data. *Lunar Planetary Science XXXVII*, CD-ROM #1517 (abstract).

Bandfield, J.L., Glotch, T.D. and Christensen, P.R. (2003) Spectroscopic identification of carbonate minerals in the martian dust. *Science*, **301**, 1084–1087.

Barrón, V. and Torrent, J. (1986) Use of the Kubelka-Munk theory to study the influence of iron oxides on soil colour. *Journal of Soil Science*, **37**, 499–510.

Bell, J.F., III, Squyres, S.W., Arvidson, R., Arneson, H.M., Bass, D., Blaney, D.L., Cabrol, N.A., Calvin, W.M., Farmer, J., Farrand, W.H., Goetz, W., Golombek, M.P., Grant, J.A., Greeley, R., Guinness, E., Hayes, A.G., Hubbard, M.Y.H., Herkenhoff, K.E., Johnson, M.J., Johnson, J.R., Joseph, J., Kinch, K.M., Lemmon, M., Madsen, M.B., Maki, J.N., Malin, M., McCartney, E., McLennan, S.M., McSween, H.Y., Jr., Ming, D.W., Moersch, J.E., Morris, R.V., Noe Dobrea, E.Z., Parker, T.J., Proton, J., Rice, J.W., Jr., Seelos, F., Soderblom, J., Soderblom, L.A., Sohl-Dickstein, J.N., Sullivan, R.J., Wolff, M.J. and Wang, A. (2004) Pancam multispectral imaging results from the Spirit rover at Gusev Crater. *Science*, **305**, 800–806.

Bibring, J.-P., Langevin, Y., Gendrin, A., Gondet, B., Poulet, F., Berthé, M., Soufflot, A., Arvidson, R., Mangold, N., Mustard, J. and Drossart, P. (2005) Mars surface diversity as revealed by the OMEGA/Mars Express observations. *Science*, **307**, 1576–1581.

Bishop, J.L. and Murad, E. (2002) Spectroscopic and geochemical analyses of ferrihydrite from hydrothermal springs in Iceland and applications to Mars. Pp. 357–370 in: *Volcano-Ice Interactions on Earth and Mars* (J.L. Smellie and M.G. Chapman, editors). Special Publication **202**, Geological Society, London.

Bishop, J.L. and Murad, E. (2005) The visible and infrared spectral properties of jarosite and alunite. *American Mineralogist*, **90**, 1100–1107.

Bishop, J.L., Pieters, C.M. and Edwards, J.O. (1994) Infrared spectroscopic analyses on the nature of water in montmorillonite. *Clays and Clay Minerals*, **42**, 701–715.

Bishop, J.L., Fröschl, H. and Mancinelli, R.L. (1998) Alteration processes in volcanic soils and identification of exobiologically important weathering products on Mars using remote sensing. *Journal of Geophysical Research*, **103**, 31,457–31,476.

Bishop, J.L., Schiffman, P. and Southard, R.J. (2002) Geochemical and mineralogical analyses of palagonitic tuffs and altered rinds of pillow lavas on Iceland and applications to Mars. Pp. 371–392 in: *Volcano-Ice Interactions on Earth and Mars* (J.L. Smellie and M.G. Chapman, editors). Special Publication **202**, Geological Society, London.

Bishop, J.L., Murad, E., Lane, M.D. and Mancinelli, R.L. (2004) Multiple techniques for mineral identification on Mars: A study of hydrothermal rocks as potential analogues for astrobiology sites on Mars. *Icarus*, **169**, 331–323.

Bishop, J.L., Dyar, M.D., Lane, M.D. and Banfield, J.F. (2005) Spectral identification of hydrated sulfates on Mars and comparison with acidic environments on Earth. *International Journal of Astrobiology*, **3**, 275–285.

Carr, M.H. (1981) *The Surface of Mars.* Yale University Press, New Haven, Connecticut, USA, 232 pp.

Chen, C.H. and Frey, F.A. (1985) Trace element and isotopic geochemistry of lavas from Haleakala volcano, East Maui, Hawaii: Implications for the origin of Hawaiian basalts. *Journal of Geophysical Research*, **90**, 8743–8768.

Chen, C.H., Frey, F.A., Garcia, M.O., Dalrymple, G.B. and Hart, S.R. (1991) The tholeiite to alkalic basalt transition at Haleakala volcano, Maui, Hawaii. *Contributions to Mineralogy and Petrology*, **106**, 183–200.

Christensen, P.R., Ruff, S.W., Fergason, R.L., Knudson, A.T., Anwar, S., Arvidson, R.E., Bandfield, J.L., Blaney, D.L., Budney, C., Calvin, W.M., Glotch, T.D., Golombek, M.P., Gorelick, N., Graff, T.G., Hamilton, V.E., Hayes, A., Johnson, J.R., McSween, H.Y., Jr., Mehall, G.L., Mehall, L.K., Moersch, J.E., Morris, R.V., Rogers, A.D., Smith, M.D., Squyres, S.W., Wolff, M.J. and Wyatt, M.B. (2004) Initial results from the Mini-TES experiment in Gusev Crater from the Spirit rover. *Science*, **305**, 837–842.

Farmer, V.C. (1974) The *Infrared Spectra of Minerals.* Monograph **4**, The Mineralogical Society, London, 539 pp.

Gendrin, A., Mangold, N., Bibring, J.-P., Langevin, Y., Gondet, B., Poulet, F., Bonello, G., Quantin, C., Mustard, J., Arvidson, R. and LeMouélic, S. (2005) Sulfates in martian layered terrains: The OMEGA/Mars Express view. *Science*, **307**, 1587–1591.

Klingelhöfer, G., Morris, R.V., Bernhardt, B., Schröder, C., Rodionov, D., de Souza, P.A.J., Yen, A.S., Gellert, R., Evlanov, E.N., Zubkov, B., Foh, J., Bonnes, U., Kankeleit,

E., Gütlich, P., Ming, D.W., Renz, F., Wdowiak, T.J., Squyres, S.W. and Arvidson, R.E. (2004) Jarosite and hematite at Meridiani Planum from Opportunity's Mössbauer spectrometer. *Science*, **306**, 1740–1745.

Lane, M.D. (2007) Midinfrared emission spectroscopy of sulfate and sulfate-bearing minerals. *American Mineralogist*, **92**, 1–18.

Lane, M.D., Dyar, M.D. and Bishop, J.L. (2004) Spectroscopic evidence for hydrous iron sulfate in the Martian soil. *Geophysical Research Letters*, **31**, L19702, doi: 10.1029/2004GL021231.

MacDonald, G.A. (1978) *Geologic map of the crater section of Haleakala National Park, Maui, Hawaii. Miscellaneous Investigations Series, Report: I-1088.* U.S. Geological Survey, 8.

Milliken, R.E. and Mustard, J.F. (2005) Quantifying absolute water content of minerals using near-infrared reflectance spectroscopy. *Journal of Geophysical Research*, **110**, E12001, doi: 10.1029/2005JE002534.

Morris, R.V., Agresti, D.G., Lauer Jr., H.V., Newcomb, J.A., Shelfer, T.D. and Murali, A.V. (1989) Evidence for pigmentary hematite on Mars based on optical, magnetic and Mössbauer studies of superparamagnetic (nanocrystalline) hematite. *Journal of Geophysical Research*, **94**, 2760–2778.

Morris, R.V., Golden, D.C., Ming, D.W., Shelfer, T.D., Jørgensen, L.C., Bell III, J.F., Graff, T.G. and Mertzman, S.A. (2001) Phyllosilicate-poor palagonitic dust from Mauna Kea volcano (Hawaii): A mineralogical analogue for magnetic Martian dust? *Journal of Geophysical Research*, **106**, 5057–5083.

Morris, R.V., Klingelhöfer, G., Schröder, C., Rodionov, D.S., Yen, A.S., Ming, D.W., de Souza, P.A.J., Fleischer, I., Wdowiak, T.J., Gellert, R., Bernhardt, B., Evlanov, E.N., Zubkov, B., Foh, J., Bonnes, U., Kankeleit, E., Gütlich, P., Renz, F., Squyres, S.W. and Arvidson, R.E. (2006) Mössbauer mineralogy of rock, soil, and dust at Gusev crater, Mars: Spirit's journey through weakly altered olivine basalt on the plains and pervasively altered basalt in the Columbia Hills. *Journal of Geophysical Research*, **111**, doi:10.1029/2005JE002584.

Murad, E. and Johnston, J.H. (1987) Iron oxides and oxyhydroxides. Pp. 507–582 in: *Mössbauer Spectroscopy Applied to Inorganic Chemistry* (G.J. Long, editor). Plenum Publishing Corporation, New York.

Parfitt, R.L., Childs, C.W. and Eden, D.N. (1988) Ferrihydrite and allophane in four andepts from Hawaii and implications for their classification. *Geoderma*, **41**, 223–241.

Poulet, F., Bibring, J.-P., Mustard, J.F., Gendrin, A., Mangold, N., Langevin, Y., Arvidson, R.E., Gondet, B. and Gomez, C. (2005) Phyllosilicates on Mars and implications for the early Mars history. *Nature*, **438**, 632–627.

Salisbury, J.W. and Wald, A. (1992) The role of volume scattering in reducing spectral contrast of reststrahlen bands in spectra of powdered minerals. *Icarus*, **96**, 121–128.

Salisbury, J.W., Walter, L.S., Vergo, N. and D'Aria, D.M. (1991) *Infrared (2.1–25 μm) Spectra of Minerals.* Johns Hopkins University Press, Baltimore, 267 pp.

Schiffman, P. and Roeske, S. (2002) Electron microprobe analysis of minerals. *Encyclopedia of Physical Sciences and Technology*, **5**, 293–306.

Schiffman, P., Spero, H.J., Southard, R.J. and Swanson, D.A. (2000) Controls on palagonitization versus pedogenic weathering of basaltic tephra: Evidence from the consolidation and geochemistry of the Keanakako'i ash member, Kilauea volcano. *Geochemistry Geophysics Geosystems*, **1**, Paper no. 2000GC000068.

Schiffman, P., Southard, R.J., Eberl, D.D. and Bishop, J.L. (2002) Distinguishing palagonitized from pedogenically-altered basaltic Hawaiian tephra: mineralogical and geochemical criteria. Pp. 393–405 in: *Volcano-Ice Interactions on Earth and Mars* (J.L. Smellie and M.G. Chapman, editors). Special Publication **202**, Geological Society, London.

Schiffman, P., Zierenberg, R.A., Marks, N., Bishop, J.L. and Dyar, M.D. (2006) Acid fog deposition at Kilauea Volcano: A possible mechanism for the formation of siliceous-sulfate rock coatings on Mars. *Geology*, **34**, 921–924.

Sherrod, D.R., Nishimitsu, Y. and Tagami, T. (2003) New K-Ar ages and the geologic evidence against rejuvenated-stage volcanism at Haleakala, East Maui, a postshield-stage volcano of the Hawaiian island chain. *Geological Society of America Bulletin*, **115**, 683–694.

Smith, P.H., Bell III, J.F., Bridges, N.T., Britt, D.T., Gaddis, L., Greeley, R., Keller, H.U., Herkenhoff, K.E., Jaumann, R., Johnson, J.R., Kirk, R.L., Lemmon, M., Maki, J.N., Malin, M.C., Murchie, S.L., Oberst, J., Parker, T.J., Reid, R.J., Sablotny, R., Soderblom, L.A., Stoker, C., Sullivan, R., Thomas, N., Tomasko, M.G., Ward, W. and Wegryn, E. (1997) Results from the Mars Pathfinder camera. *Science*, **278**, 1758–1765.

Squyres, S.W., Arvidson, R.E., Bell, J.F., III, Brückner, J., Cabrol, N.A., Calvin, W.M., Carr, M.H., Christensen, P.R., Clark, B.C., Crumpler, L., Des Marais, D.J., d'Uston, C., Economou, T., Farmer, J., Farrand, W.H., Folkner, W., Golombek, M.P., Gorevan, S., Grant, J.A., Greeley, R., Grotzinger, J., Haskin, L.A., Herkenhoff, K.E., Hviid, S., Johnson, J., Klingelhöfer, G., Knoll, A., Landis, G., Lemmon, M., Li, R., Madsen, M.B., Malin, M.C., McLennan, S.M., McSween, H.Y., Jr., Ming, D.W., Moersch, J., Morris, R.V., Parker, T.J., Rice, J.W., Jr., Richter, L., Rieder, R., Sims, M., Smith, M., Smith, P., Soderblom, L.A., Sullivan, R., Wänke, H., Wdowiak, T.J., Wolff, M.J. and Yen, A.S. (2004a) The Spirit rover's Athena science investigation at Gusev Crater, Mars. *Science*, **305**, 794–799.

Squyres, S.W., Arvidson, R.E., Bell, J.F., III, Brückner, J., Cabrol, N.A., Calvin, W.M., Carr, M.H., Christensen, P.R., Clark, B.C., Crumpler, L., Des Marais, D.J., d'Uston, C., Economou, T., Farmer, J., Farrand, W.H., Folkner, W., Golombek, M.P., Gorevan, S., Grant, J.A., Greeley, R., Grotzinger, J., Haskin, L.A., Herkenhoff, K.E., Hviid, S., Johnson, J., Klingelhöfer, G., Knoll, A., Landis, G., Lemmon, M., Li, R., Madsen, M.B., Malin, M.C., McLennan, S.M., McSween, H.Y., Jr., Ming, D.W., Moersch, J., Morris, R.V., Parker, T.J., Rice, J.W., Jr., Richter, L., Rieder, R., Sims, M., Smith, M., Smith, P., Soderblom, L.A., Sullivan, R., Wänke, H., Wdowiak, T.J., Wolff, M.J. and Yen, A.S. (2004b) The Opportunity rover's Athena science investigation at Meridiani Planum, Mars. *Science*, **306**, 1698–1703.

Stanjek, H. and Friedrich, R. (1986) The determination of layer charge by curve-fitting of Lorentz- and polarization-corrected X-ray diagrams. *Clay Minerals*, **21**, 183–190.

Stearns, H. T. (1942) Origin of Haleakala Crater, Island of Maui, Hawaii. *Geological Society of America Bulletin*, **53**, 1–13.

Wivel, C. and Mørup, S. (1981) Improved computational procedure for evaluation of overlapping hyperfine parameters distributions in Mössbauer spectra. *Journal of Physics*, **E14**, 605–610.

(*Received 16 February 2006; revised 30 August 2006; Ms. 1143; A.E. Peter J. Heaney*)